INDIAN JOURNAL OF SCIENCE AND TECHNOLOGY

Check for updates

*Corresponding author.

aditya_sharma18391@yahoo.in

Small Signal Modelling and Stability Analysis of a Grid Connected Inverted Based Microgrid

Aditya Sharma[1]*, **D K Palwalia**[2]

1 Research Scholar, Electrical Department, Rajasthan Technical University, Kota, Rajasthan, India
2 Professor, Electrical Department, Rajasthan Technical University, Kota, Rajasthan, India

Abstract

Objectives: This work focuses on the stability analysis of grid connected microgrids. It considers the impact of load disturbance and grid voltage change on voltage and current levels, as well as reactive and active power responses, is analysed. **Methods:** A comprehensive small-signal state-space model is developed for an inverter-based microgrid, incorporating submodules of inverters, phase-locked loops (PLLs), and LCL filters. The model is linearized around a stable operating point, and eigenvalue analysis is performed and validated through MATLAB/Simulink simulations. A current controller operating in the d-q frame is proposed to enhance stable power conversion and maintain microgrid stability. **Findings:** The proposed model and control strategy demonstrate the microgrid's ability to maintain transient voltage stability under severe dynamic conditions. During a 10% grid voltage fluctuation, the microgrid exhibits stable active and reactive power responses, with currents and voltages at the point of common coupling stabilizing within 0.2 seconds. Furthermore, when a 25 kVA active load is disconnected, the microgrid effectively manages the power transition, maintaining stable operation with minimal deviations in key parameters. The current controller simplifies AC current control, integrating active power management from solar input, DC-link voltage stability, and reactive power control. **Novelty:** The novelty lies in the comprehensive analysis of transient voltage stability in grid-connected microgrids under grid voltage fluctuations and load disturbances, areas that have received limited attention in previous research. By developing a detailed small-signal state-space model incorporating PLL and LCL filter dynamics and proposing a robust control strategy with the current controller, this study offers new insights into enhancing the resilience and reliability of grid-connected microgrids during transient events.

Keywords: Microgrid; Small Signal Stability; Voltage Source Inverter; State Space model; Eigen Values

1 Introduction

Emerging developments in localized power generation systems on a smaller scale, coupled with progress in power electronics, have paved the way for concepts in upcoming network technologies like microgrids. These compact, self-contained segments within power systems hold the potential to elevate dependability and effectiveness and play a pivotal role in seamlessly integrating renewable energy and various modes of distributed generation (DG)[1].

Fuel cells, photovoltaic and microturbines are among the types of distributed generations connected to the network through power electronics converters. These converters give these sources more flexibility in how they work and are controlled, unlike traditional machines[2]. These converters could cause oscillations in the system when there are disturbances due to negligible physical inertia in them. Under grid connected mode, behaviour of microgrid is largely influenced by main grid due to relatively small size of the micro sources[3]. Control methods and stability analyses for grid integration of distributed generation units is seen as one of the most accomplished through the use of microgrid[4]. Considering that microgrid has significantly less physical inertia than the main grid, even minor disruptions like variations in the power output from photovoltaic arrays or wind turbines, as well as the connection or disconnection of local loads, can give rise to concerns about power quality and stability[5]. In particular, the frequency and voltage levels within microgrid might experience various that may lead to a decline in the overall stability of the system[6]. Efficient way for integrating distributed energy resources into microgrids with stable control systems are discussed[7].

While microgrids offer benefits such as dynamic islanding during faults and voltage dips, and improved value proposition for utilities and customers, several technical challenges remain unaddressed. Previous studies have explored control schemes for inverter-based microgrids[8], variable droop methods for improved frequency control and load sharing[9], droop control approaches for islanding detection[10] and algorithms to mitigate frequency distortion and voltage drop issues[11]. In grid-connected mode, Phase-Locked Loops (PLLs) are crucial for synchronizing the inverter's output with the grid, ensuring stable power flow, while LCL filters are essential for reducing harmonic distortions and maintaining power quality. Although some research has been conducted on modelling and steady-state analysis of islanded microgrids[12], the dynamics of PLLs and filters have received limited attention[13]. Furthermore, while small-signal stability analysis of grid-connected microgrids has been explored[14], transient stability analysis during grid voltage fluctuations and load disturbances remains largely unexplored. Existing studies on grid-connected microgrids have primarily focused on steady-state conditions, overlooking the transient behaviour during disturbances[15]. While efforts have been made to improve the stability of grid-side converters under weak grid conditions[16] and address LCL filter resonance issues[17], a comprehensive analysis of transient voltage stability considering the combined effects of grid voltage fluctuations, load disturbances, and the dynamics of PLLs and LCL filters is lacking. While extensive research has been conducted on microgrid stability during islanded mode, considering factors such as control parameters and load variations, limited attention has been given to transient stability analysis of grid-connected microgrids under dynamic conditions, such as grid voltage fluctuations and load disturbances. These disturbances can significantly impact the stability of grid-connected microgrids, as they are generally considered stable due to the dominant influence of the main grid.

This work addresses this research gap by investigating the transient voltage stability of a grid-connected microgrid under grid voltage fluctuations and load disturbances. A comprehensive small-signal state-space model of the microgrid is developed, incorporating submodules of inverters and their individual state-space equations, combined in a common reference frame. The complete microgrid model is linearized around a stable operating point, and eigenvalue analysis is performed and validated against MATLAB/Simulink simulations. Furthermore, a current controller is proposed in the inverter control scheme to enhance stable power conversion and maintain microgrid stability during grid voltage fluctuations and load disturbances. Operating in the d-q frame, this controller simplifies AC current control, integrating active power management from solar input, DC-link voltage stability, and reactive power control. Through simulations involving grid voltage alterations and load disturbances, the transient voltage stability of the microgrid is evaluated with the proposed controller. The results demonstrate the microgrid's ability to maintain stability, as evidenced by the stabilization of active and reactive power, currents, and voltages at the point of common coupling.

2 Methodology

System Description

A control design for a microgrid is presented in this paper, which can operate in either grid-connected mode or islanded mode. However, it focuses solely on the grid-connected mode of operation. In this configuration, the PV system is directly connected to an inverter, which, in turn, is connected to the grid through filters as shown in Figure 1. The mode of operation is determined by a switch located at the point of common coupling (PCC) between the grid and the inverter.

The inverter's output is passed through an LCL filter, which eliminates high-frequency switching disturbances. Subsequently, the voltage and current, once filtered, are transformed into dq-axis components via a Clarke reference frame transformation. These transformed measurements are used to determine the output power of the inverter. This calculated power is then subjected to a low-pass filter that removes any high-frequency interference before it is sent to the power controller. Under power controller power calculated at the input side of inverter is compared with the measured total power after filter, error is further processed to receive reference limit voltage across inverter capacitor. This reference voltage along with the reference DC voltage from Maximum point tracking technique (MPPT) is passed through voltage controller which produces limit current for capacitor current and DC voltage at the inverter input. Current reference signals derived from the Maximum Power Point Tracking (MPPT) are matched against the respective measured currents of the filter inductor, subsequently being processed by a set of Proportional-Integral (PI) controllers to generate voltage commands. These command voltages then appear at the LCL filter's input. The inverter is connected to the bus through the filter's coupling inductor. This voltage commanded signal is transformed into abc frame using Clarke transformation and is fed into space vector pulse width modulation (SVPWM) which produces PWM pulses for voltage source inverter. A resistor positioned in series with the filter's capacitor provides the necessary damping for the resonant frequency related to the output filter.

In a dq-based Phase-Locked Loop (PLL), the system's frequency is determined by setting the d-axis voltage component to zero. The PLL serves a dual purpose: it measures the system's frequency and also determines the voltage's phase angle. This angle is instrumental in performing conversions between stationary and synchronous reference frames. The dynamics of the inverters are regulated by several components: the output filter, the coupling inductor, the computation of average power, the PLL, as well as the voltage and current controllers, all of which are modelled within the individual reference frame of each inverter as specified by the phase angle measured by the PLL. System parameters are listed in Table 1.
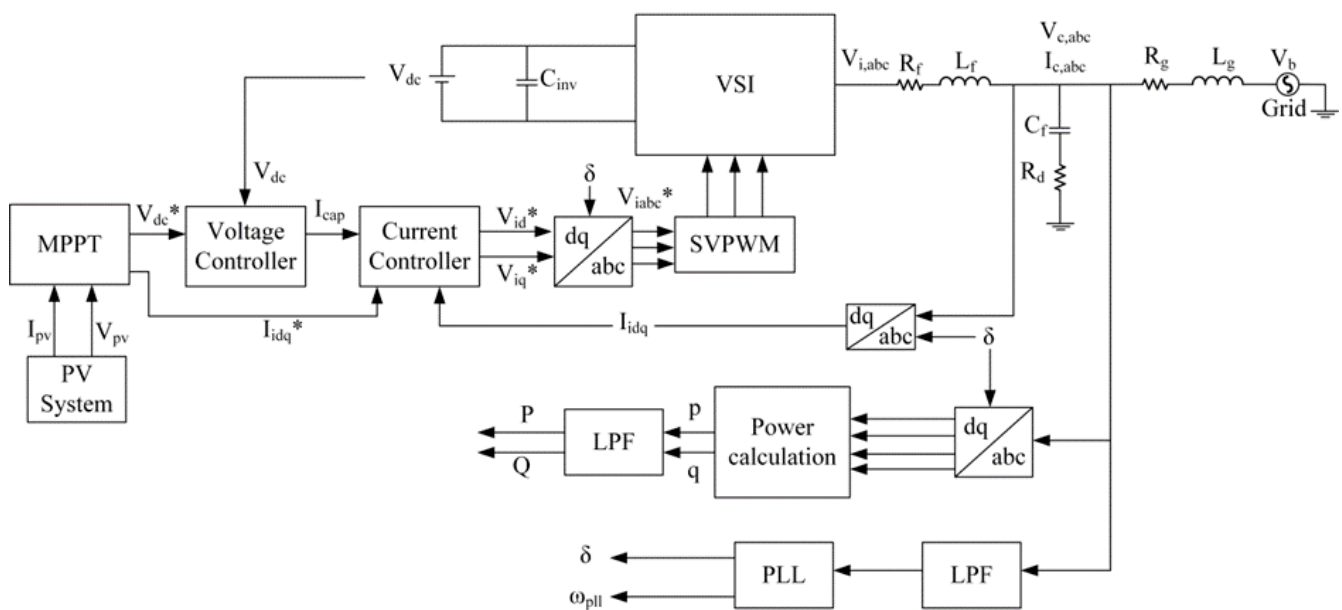
Fig 1. Proposed control strategy of microgrid

Table 1. System Parameters

Parameter	Value	Parameter	Value
DC Link voltage (V_{dc})	700 V	Damping Resistance (R_d)	3 Ω
PV voltage (V_{pv})	700 V	PLL constant (Kp_{pll})	0.9428
System frequency (ω_{sys})	314.15 rad/sec	LPF cut-off frequency (ω_c)	100 kHZ
Switching frequency (f_{sw})	10 kHZ	PLL operating frequency ($\omega_{c,pll}$)	7853.98 rad/sec
DC Link Capacitor (C_{inv})	100 x 10^{-3} F	Current Controller Constant (K_c, T_c)	1.880, 1.58 x 10^{-3}
Filter Inductor (L_f), Resistance (R_f),	4.20 mH, 0.5 Ω,	Voltage Controller Constant (K_v, T_v)	3.571, 5.2 x 10^{-4}
Filter Capacitance (C_f)	50 μF	Grid Side Inductor (L_g), Resistance (R_g)	0.50 mH, 0.09 Ω

System Modelling

Complete state space small signal model of the system is presented into five submodules. Each submodule is linearized and represented in the state space form and a complete microgrid system small signal model is formed by combining all of the submodules on a common reference frame.

2.1 Solar PV

The fundamental component of a photovoltaic (PV) generator is the solar cell, a P-N semiconductor junction converting solar radiation directly into DC current through the photovoltaic effect[18]. It consists of photo current (I_{ph}) which is driven by temperature and irradiation, shunt resistance (I_{sh}) which describes leakage current. The load current is given as:

$$I = I_{ph} - I_D - I_{sh} \tag{1}$$

$$I_{ph} = [I_{sc} + K_i (T_k - T)] \times \frac{G}{1000} \tag{2}$$

$$I_{RS} = \frac{I_{sc}}{[exp\left(q \times \frac{V}{N_s} \times k \times A \times T\right) - 1]} \tag{3}$$

$$I_D = I_{RS} \left[\frac{T}{T_r}\right]^3 exp\left[\frac{q \times E_{go}}{AK}\left\{\frac{1}{T_r} - \frac{1}{T}\right\}\right] \tag{4}$$

$$I_{PV} = N_P \times I_{Ph} - N_P \times I_D \left[exp\left\{\frac{q \times V \times + I_{PV}R_s}{N_s \times AkT}\right\} - 1\right] \tag{5}$$

Where, I_{PV} represents the current flowing through the diode, while I_D denotes the diode's reverse saturation current. I_{sh} refers to the leakage current, and V_{PV} stands for the voltage across the diode. V indicates the voltage when the circuit is open, R_s is the resistance in series with the diode, and R_{sh} is the resistance across the shunt. I_{sc} is the short circuit current, q symbolizes the charge of an electron, and k represents the Boltzmann constant. A signifies the diode ideality factor, and T is the temperature at the p-n junction. N_P and N_s are the counts of cells connected in parallel and in series, respectively. Solar PV output is maximised using MPPT technique with Perturbation & Observation (P&O) method[19].

2.2 Power states

Instantaneous active power (p) and reactive power (q) generated by the inverter is measured by calculating the dq axis output of voltage and current. Active and reactive power is represented as:

$$p = \frac{3}{2}(V_{cd}i_{cd} + V_{cq}i_{cq}) \tag{6}$$

$$q = \frac{3}{2}(V_{cd}i_{cq} - V_{cq}i_{cd}) \tag{7}$$

V_{cdq} and i_{cdq} are the voltage and current in dq axis at PCC. Instantaneous power is passed through a low pass filter (LPF) with the cut off frequency (ω_c) to obtain active and reactive power.

$$P = \frac{\omega_c}{s + \omega_c}p \text{ and } Q = \frac{\omega_c}{s + \omega_c}q \tag{8}$$

From above Equations (6), (7) and (8) states for power can be determined,

$$\dot{P} = -P\omega_c + 1.5\omega_c (V_{cd}i_{gd} + V_{cq}i_{gq}) \tag{9}$$

$$\dot{Q} = -Q\omega_c + 1.5\omega_c \left(V_{cd} i_{gq} - V_{cq} i_{gd} \right) \tag{10}$$

$\triangle P$ and $\triangle Q$ are small power variations from operating point, P and Q from Equations (9) and (10). $\triangle I_{idq}$, $\triangle V_{cdq}$ and $\triangle I_{cdq}$ are small variations of voltage and current with respect to their respective operating points. Thus, the small signal dynamic model of power control is given by:

$$\begin{bmatrix} \dot{\triangle P} \\ \dot{\triangle Q} \end{bmatrix} = A_P \begin{bmatrix} \triangle P \\ \triangle Q \end{bmatrix} + B_P \begin{bmatrix} \triangle I_{idq} \\ \triangle V_{cdq} \\ \triangle I_{cdq} \end{bmatrix} \tag{11}$$

$$\begin{bmatrix} \triangle p \\ \triangle q \end{bmatrix} = C_P \begin{bmatrix} \triangle P \\ \triangle Q \end{bmatrix} + D_P \begin{bmatrix} \triangle I_{idq} \\ \triangle V_{cdq} \\ \triangle I_{cdq} \end{bmatrix} \tag{12}$$

$$A_P = \begin{bmatrix} -\omega c & 0 \\ 0 & -\omega c \end{bmatrix} \quad B_P = 1.5\omega c \begin{bmatrix} 0 & 0 & I_{cd} & I_{cq} & V_{cd} & V_{cq} \\ 0 & 0 & -I_{cq} & I_{cd} & V_{cq} & -V_{cd} \end{bmatrix}$$

$$C_P = \begin{bmatrix} 0 & 0 \\ 0 & 0 \end{bmatrix} \quad D_P = 1.5 \begin{bmatrix} 0 & 0 & I_{cd} & I_{cq} & V_{cd} & V_{cq} \\ 0 & 0 & -I_{cq} & I_{cd} & V_{cq} & -V_{cd} \end{bmatrix} \tag{13}$$

2.3 Phase Locked Loop (PLL)

In order to provide current with a power factor of one and ensure alignment with the grid, the PV system requires information about the grid's phase angle, voltage, and frequency. The microgrid system is modelled in dq frame, hence filter dynamic model is also derived in dq frame. A dq based PLL has been chosen [20]. Only the q component of the voltage measured after the filter capacitor is used as the input in PLL so that phase is locked such that $V_{oq} = 0$. $K_{p,PLL}$ and $K_{i,PLL}$ are the proportional and integral constant of PI controller. δ and ω_{PLL} are the phase angle and inverter frequency respectively. Block diagram for PLL is mentioned in Figure 2 and following are the three states relevant for PLL:
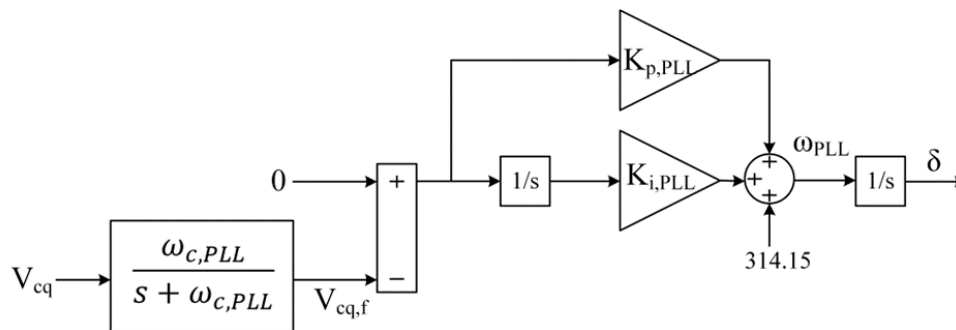

Fig 2. Block diagram PLL structure

From Figure 2, the following equations can be formed

$$\dot{V}_{cq,f} = \omega_{cPLL} V_{cq} - \omega_{cPLL} V_{cq,f} \tag{14}$$

$$\dot{\varphi}_{PLL} = -V_{cq,f} \tag{15}$$

$$\dot{\delta} = \omega_{PLL} \tag{16}$$

$$\omega_{PLL} = 314.15 - K_{p,PLL}V_{cq,f} + K_{i,PLL}\varphi_{PLL} \tag{17}$$

The state space model matrix of PLL is given as follows:

$$\begin{bmatrix} \triangle\dot{V}_{cd,f} \\ \triangle\dot{\varphi}_{PLL} \\ \triangle\dot{\delta} \end{bmatrix} = A_{PLL} \begin{bmatrix} \triangle V_{cd,f} \\ \triangle\varphi_{PLL} \\ \triangle\delta \end{bmatrix} + B_{PLL} \begin{bmatrix} \triangle I_{idq} \\ \triangle V_{cdq} \\ \triangle I_{cdq} \end{bmatrix} \tag{18}$$

$$[\triangle\omega_{PLL}] = C_{PLL} \begin{bmatrix} \triangle V_{cd,f} \\ \triangle\varphi_{PLL} \\ \triangle\delta \end{bmatrix} + D_{PLL} \begin{bmatrix} \triangle I_{idq} \\ \triangle V_{cdq} \\ \triangle I_{cdq} \end{bmatrix} \tag{19}$$

$$A_{PLL} = \begin{bmatrix} \omega_{c,PLL} & 0 & 0 \\ -1 & 0 & 0 \\ -K_{P,PLL} & K_{i,PLL} & 0 \end{bmatrix} \quad B_{PLL} = \begin{bmatrix} 0 & 0 & -\omega_{c,PLL} & 0 & 0 & 0 \\ 0 & 0 & 0 & 0 & 0 & 0 \\ 0 & 0 & 0 & 0 & 0 & 0 \end{bmatrix}$$

$$C_{PLL} = \begin{bmatrix} -K_{P,PLL} & K_{i,PLL} & 0 \end{bmatrix} \quad D_{PLL} = \begin{bmatrix} 0 & 0 & 0 & 0 & 0 & 0 \end{bmatrix} \tag{20}$$

2.4 Voltage Controller

The voltage controller's main function is to maintain the DC-link voltage at its desired reference value, V_{dc}^*. The controller compares this reference value with the actual DC-link voltage, V_{dc} to generate an error signal. This error signal is then processed through a PI controller to produce a reference current for the DC-link capacitor, I_{dcap} as shown in Figure 3. K_v and T_v are proportional gain and integral time constant.
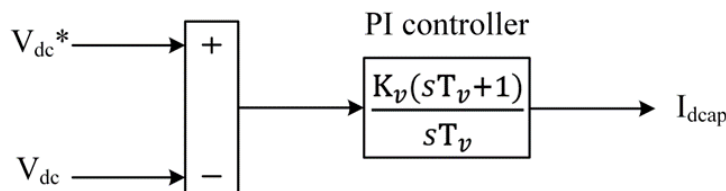
Fig 3. Block diagram of voltage controller

The corresponding state equations are:

$$I_{dcap} = K_v(V_{dc}^* - V_{dc}) + \frac{K_v}{T_v}(\varphi_d) \tag{21}$$

$$\dot{\varphi_d} = V_{dc}^* - V_{dc} \tag{22}$$

Using Equations (21) and (22), small signal dynamic model of voltage controller is presented as:

$$[\triangle\dot{\varphi}_d] = A_V [\triangle\varphi_d] + B_{V1} \begin{bmatrix} \triangle I_{id} \\ \triangle I_{iq} \\ \triangle V_{cd} \\ \triangle V_{cq} \\ \triangle I_{cd} \\ \triangle I_{cq} \end{bmatrix} + B_{V2} \begin{bmatrix} V_{dc}^* \\ V_{dc} \end{bmatrix} \tag{23}$$

$$[\triangle I_{dcap}] = C_V \left[\triangle \varphi_d\right] + D_{V1} \begin{bmatrix} \triangle I_{id} \\ \triangle I_{iq} \\ \triangle V_{cd} \\ \triangle V_{cq} \\ \triangle I_{cd} \\ \triangle I_{cq} \end{bmatrix} + D_{V2} \begin{bmatrix} V_{dc}^* \\ V_{dc} \end{bmatrix} \tag{24}$$

$$A_V = [0] \quad B_{V1} = [0] \quad B_{V2} = \begin{bmatrix} 1 & -1 \end{bmatrix} \tag{}$$

$$C_V = \begin{bmatrix} \dfrac{K_v}{T_v} \end{bmatrix} \quad D_{V1} = [0] \quad D_{V2} = \begin{bmatrix} K_v & -K_v \end{bmatrix} \tag{25}$$

2.5 Current control

The current controller's purpose is to regulate the inverter currents, ensuring that they follow the desired references. This controller takes two main inputs for the d-axis: the reference current I_{pv} from the MPPT and I_{dcap} from the voltage controller. The combined d-axis reference becomes $I_{pv} + I_{dcap}$. For the q-axis, the objective is usually to regulate the current to zero, making the reference $I_{iq}^* = 0$. The errors in the d and q axes are computed and then fed into separate PI controllers, yielding the control voltages V_{id}^* and V_{iq}^* accordingly as shown in Figure 4. From the MPPT, we have I_{pv}, which can be used as I_{id}^* for the current controller. So,

$$I_{id}^* = I_{pv} \tag{26}$$

Now, the current controller will take both I_{id}^* (from MPPT) and I_{dcap} (from voltage controller) to determine the appropriate modulation signals for the inverter. K_c and T_c are proportional gain and integral time constant. Cross coupling and feed forward compensation terms are included in the controller to ensure accurate and dynamic tracking of the inverter's currents in the presence of grid inductance.
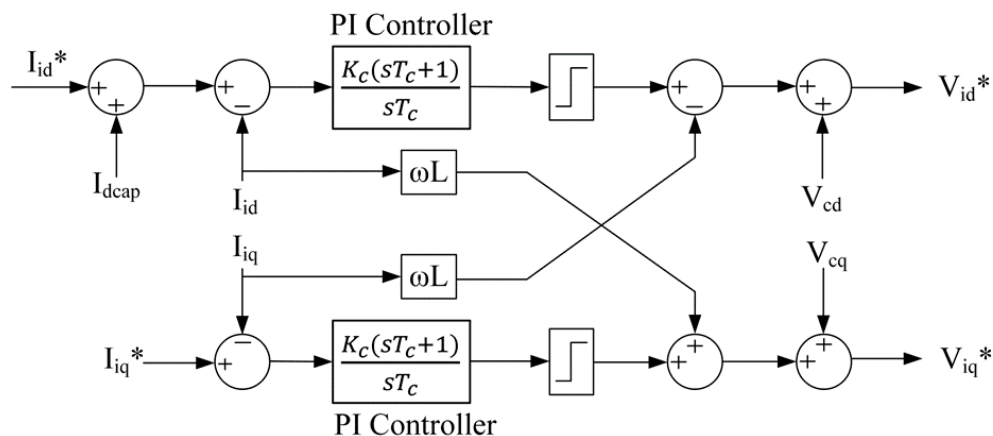

Fig 4. Block diagram of current control loop

Following equations represents the linearized small signal state space form of current controller:

$$\dot{\gamma}_d = I_{id}^* + I_{dcap} - I_{id} \tag{27}$$

$$\dot{\gamma}_q = I_{iq}^* - I_{iq} \tag{28}$$

$$V_{id}^* = K_c \left(I_{id}^* + I_{dcap} - I_{id} \right) + \frac{K_c}{T_c} \left(\gamma_d \right) - \omega L_f I_{iq} + V_{cd} \tag{29}$$

$$V_{iq}^* = K_c \left(I_{iq}^* - I_{iq} \right) + \frac{K_c}{T_c} \left(\gamma_q \right) + \omega L_f I_{iq} + V_{cd} \tag{30}$$

$$\begin{bmatrix} \triangle \dot{\gamma}_d \\ \triangle \dot{\gamma}_q \end{bmatrix} = A_C \begin{bmatrix} \triangle \gamma_d \\ \triangle \gamma_q \end{bmatrix} + B_{C1} \begin{bmatrix} \triangle I_{id} \\ \triangle I_{iq} \\ \triangle V_{cd} \\ \triangle V_{cq} \\ \triangle I_{cd} \\ \triangle I_{cq} \end{bmatrix} + B_{C2} \begin{bmatrix} \triangle I_{id}^* \\ \triangle I_{iq}^* \\ \triangle I_{dcap} \end{bmatrix} \tag{31}$$

$$\begin{bmatrix} \triangle V_{id}^* \\ \triangle V_{iq}^* \end{bmatrix} = C_C \begin{bmatrix} \triangle \gamma_d \\ \triangle \gamma_q \end{bmatrix} + D_{C1} \begin{bmatrix} \triangle I_{id} \\ \triangle I_{iq} \\ \triangle V_{cd} \\ \triangle V_{cq} \\ \triangle I_{cd} \\ \triangle I_{cq} \end{bmatrix} + D_{C2} \begin{bmatrix} \triangle I_{id}^* \\ \triangle I_{iq}^* \\ \triangle I_{dcap} \end{bmatrix} \tag{32}$$

$$A_C = \begin{bmatrix} 0 & 0 \\ 0 & 0 \end{bmatrix} \quad B_{C1} = \begin{bmatrix} -1 & 0 & 0 & 0 & 0 & 0 \\ 0 & -1 & 0 & 0 & 0 & 0 \end{bmatrix} \quad B_{C2} = \begin{bmatrix} 1 & 0 & 1 \\ 0 & 1 & 0 \end{bmatrix}$$

$$C_C = \begin{bmatrix} \frac{K_c}{T_c} & 0 \\ 0 & \frac{K_c}{T_c} \end{bmatrix} \quad D_{C1} = \begin{bmatrix} -K_c & -\omega L_f & 1 & 0 & 0 & 0 \\ \omega L_f & -K_c & 1 & 0 & 0 & 0 \end{bmatrix}$$

$$D_{C2} = \begin{bmatrix} K_c & 0 & K_c \\ 0 & K_c & 0 \end{bmatrix} \tag{33}$$

2.6 LCL filter

In order to reduce the high-frequency current harmonics, LCL filters are used in most applications. The microgrid model is in dq frame, hence filter dynamic model is also derived in dq frame. Filter used in this microgrid is shown in Figure 5. We assumed that the commanded voltage $(V_{i,dq}^*)$ appears at the input of the filter inductor, $V_{i,dq}^* = V_{i,dq}$. Under this approach all the IGBT and diodes losses are neglected. The resistors R_f, R_c are the parasitic resistance of the inductors. Passive damping using a damping resistor (R_d) in series with the filter capacitor is often employed to further suppress the resonance frequency and enhance the stability of the LCL filter shown below. Filter inductance and filter capacitance is represented by L_f and C_f.

The state equations governing the filter dynamics are as follows:

$$\dot{I}_{id} = \frac{1}{L_f} \left(-R_i I_{id} + V_{id} - V_{cd} \right) + \omega_{pll} I_{iq} \tag{34}$$

$$\dot{I}_{iq} = \frac{1}{L_f} \left(-R_i I_{iq} + V_{iq} - V_{cq} \right) - \omega_{pll} I_{id} \tag{35}$$

$$\dot{I}_{cd} = \frac{1}{L_g} \left(-R_g I_{cd} + V_{cd} - V_{bd} \right) + \omega_{pll} I_{cq} \tag{36}$$
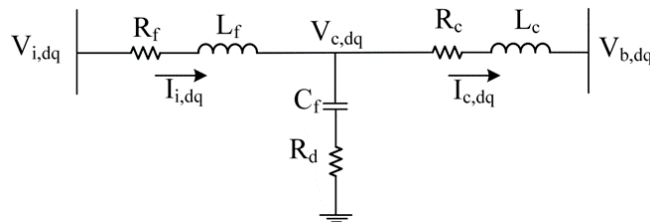
Fig 5. LCL Filter

$$\dot{I}_{cq} = \frac{1}{L_g}\left(-R_g I_{cq} + V_{cq} - V_{bq}\right) - \omega_{pll} I_{cd} \tag{37}$$

$$\dot{V}_{cd} = \frac{1}{C_f}\left(I_{id} - I_{cd}\right) + \omega_{pll} V_{cq} + R_d(\dot{I}_{id} - \dot{I}_{cd}) \tag{38}$$

$$\dot{V}_{cq} = \frac{1}{C_f}\left(I_{iq} - I_{cq}\right) - \omega_{pll} V_{cd} + R_d(\dot{I}_{iq} - \dot{I}_{cq}) \tag{39}$$

In this set of equations, ω_{pll} is the operating frequency of system that is generated by PLL. The following equations represent the linearized small signal state space form of LCL filter with ω_{pll} as the system frequency.

$$\begin{bmatrix} \triangle\dot{I}_{id} \\ \triangle\dot{I}_{iq} \\ \triangle\dot{V}_{cd} \\ \triangle\dot{V}_{cq} \\ \triangle\dot{I}_{cd} \\ \triangle\dot{I}_{cq} \end{bmatrix} = A_{LCL}\begin{bmatrix} \triangle I_{id} \\ \triangle I_{iq} \\ \triangle V_{cd} \\ \triangle V_{cq} \\ \triangle I_{cd} \\ \triangle I_{cq} \end{bmatrix} + B_{LCL1}\begin{bmatrix} \triangle V_{id} \\ \triangle V_{iq} \end{bmatrix} + B_{LCL2}\begin{bmatrix} \triangle V_{bd} \\ \triangle V_{bq} \end{bmatrix} + B_{LCL3}[\triangle\omega_{PLL}] \tag{40}$$

$$A_{LCL} = \begin{bmatrix} -\left(\frac{R_i+R_d}{L_i}\right) & \omega_{PLL} & -\frac{1}{L_i} & 0 & \frac{R_d}{L_i} & 0 \\ -\omega_{PLL} & -\left(\frac{R_i+R_d}{L_i}\right) & 0 & -\frac{1}{L_i} & 0 & \frac{R_d}{L_i} \\ \frac{1}{C_f} & 0 & 0 & \omega_{PLL} & -\frac{1}{C_f} & 0 \\ 0 & \frac{1}{C_f} & -\omega_{PLL} & 0 & 0 & -\frac{1}{C_f} \\ \frac{R_d}{L_g} & 0 & \frac{1}{L_g} & 0 & -\left(\frac{R_g+R_d}{L_i}\right) & \omega_{PLL} \\ 0 & \frac{R_d}{L_g} & 0 & \frac{1}{L_g} & -\omega_{PLL} & -\left(\frac{R_g+R_d}{L_i}\right) \end{bmatrix}$$

$$B_{LCL1} = \begin{bmatrix} \frac{1}{L_i} & 0 \\ 0 & \frac{1}{L_i} \\ 0 & 0 \\ 0 & 0 \\ 0 & 0 \\ 0 & 0 \end{bmatrix} \quad B_{LCL2} = \begin{bmatrix} 0 & 0 \\ 0 & 0 \\ 0 & 0 \\ 0 & 0 \\ -\frac{1}{L_g} & 0 \\ 0 & -\frac{1}{L_g} \end{bmatrix} \quad B_{LCL3} = \begin{bmatrix} I_{iq} \\ -I_{id} \\ V_{cq} \\ -V_{cd} \\ I_{cq} \\ -I_{cd} \end{bmatrix} \tag{41}$$

2.7 Complete Model of Inverter

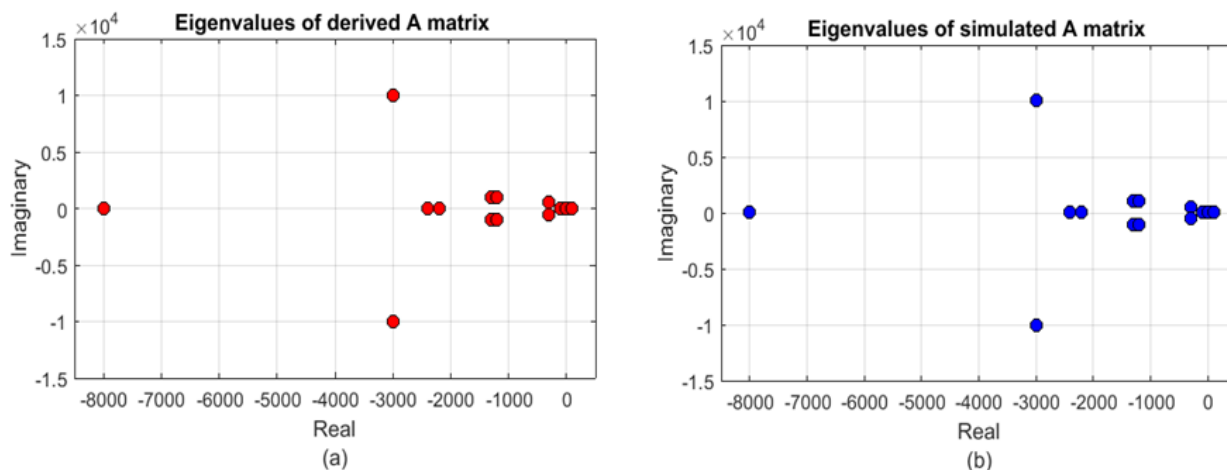The frequency of the Phase-Locked Loop (PLL), which matches the frequency of the inverter, is used as the standard frame of reference for the entire system. Consequently, every equation is formulated based on the inverter's frame of reference. An exception to this is the voltage present at the grid bus, which must undergo a conversion utilizing a specified transformation matrix mentioned in Equations (42) and (45). According to Equation (45), the grid voltage undergoes a transformation to align with the common reference frame, and within this transformation, the angle δ is employed to denote the difference in phase angle between the grid and inverter voltages. Equations are linearized and state space form is represented as:

$$[\triangle I_{cDQ}] = [T_s]\left[\triangle I_{cdq}\right] + [T_c][\triangle\delta] \tag{42}$$

$$T_s = \begin{bmatrix} cos(\delta) & -sin(\delta) \\ sin(\delta) & cos(\delta) \end{bmatrix} \tag{43}$$

$$T_c = \begin{bmatrix} -I_{cd}sin(\delta) & -I_{cq}cos(\delta) \\ I_{cd}cos(\delta) & -I_{cq}sin(\delta) \end{bmatrix} \tag{44}$$

$$\left[\triangle V_{bdq}\right] = \left[T_s^{-1}\right]\left[\triangle V_{bDQ}\right] + \left[T_v^{-1}\right][\triangle\delta] \tag{45}$$

$$T_v^{-1} = \begin{bmatrix} -V_{bD}sin(\delta) & V_{bQ}cos(\delta) \\ -V_{bD}cos(\delta) & -V_{bQ}sin(\delta) \end{bmatrix} \tag{46}$$

A complete state space small signal model of the microgrid is obtained by combining the individual states of power controller, PLL, voltage controller, current controller and LCL filter from Equations (11), (12), (18), (19), (23), (24), (31), (32), (40), (42) and (45). There are 14 states, 2 inputs and 2 outputs for the system.

$$\left[\triangle\dot{x}_{inv}\right] = A_{INV}\left[\triangle x_{inv}\right] + B_{INV}\left[\triangle u_{inv}\right] \tag{47}$$

A_{INV} represents the state matrix of complete model and B_{INV} represents the input matrix to the system. $\triangle x_{inv}$ are the total states associated with the system and $\triangle u_{inv}$ are the inputs for inverter.

$$\triangle x_{inv} = \begin{pmatrix} P & Q & V_{cd,f} & \varphi_{PLL} & \delta & \varphi_d & \gamma_d & \gamma_q & I_{id} & I_{iq} & V_{cd} & V_{cq} & I_{cd} & I_{cq} \end{pmatrix}^T \tag{48}$$

$$\triangle u_{inv} = V_{bDQ} = \begin{pmatrix} V_{bD} & V_{bQ} \end{pmatrix}^T \tag{49}$$

$$A_{INV} = \begin{bmatrix} A_P & 0 & 0 & 0 & B_P \\ B_{PLL}C_P & A_{PLL} & 0 & 0 & B_{PLL} \\ B_C D_{V1} C_P & B_{V1} C_{PLL} & A_V & 0 & B_{V2} \\ B_{LCL1}D_{C1}D_{V1}C_P+ & B_{C1}D_{V1}C_{PLL} & B_{C1}C_V & A_C & B_{C1}D_{V2}+B_{C2} \\ B_{LCL3}C_P+B_{LCL2}\begin{bmatrix}T_V^{-1} & 0 & 0\end{bmatrix} & B_{LCL}D_{c1}D_{V1}C_{PLL} & B_{LCL1}D_{C1}C_V & B_{LCL1}C_C & A_{LCL}+B_{LCL1}(D_{C1}D_{V1}+D_{C2}) \end{bmatrix}_{14\times 14} \tag{50}$$

After linearization of the entire small signal model of microgrid around the stable operating point, the eigenvalue analysis has been done. The eigenvalue plot shown in Figure 6(a) and (b) are from developed linearized model and Simulink linmod command respectively. It can be observed that the results from simulink model match with the developed linearized model. It is observed the introduction of a damping resistor in an LCL filter of a microgrid model leads to a more stable system, with eigenvalues moved towards the left half-plane, indicating better damping and reduced risk of oscillatory behaviour.

The comparison of eigenvalues derived from a linearized model with those from a Simulink model reveals consistency, indicating the linearized model accurately represents the Simulink system's dynamics as shown in Table 2 below. Almost all eigenvalues have negative real parts, signifying stability; however, the presence of a positive eigenvalue suggests a potential for system instability, warranting further investigation or the implementation of control strategies to maintain stability. Complex eigenvalues with negative real parts indicate the system exhibits damped oscillations, with the oscillatory behaviour diminishing over time. The eigenvalue with the largest negative real part suggests rapid system dynamics, while those closer to zero imply slower responses.

Fig 6. Eigenvalue plot using (a) linearized model and (b) simulink model

Table 2. Eigen values comparison

S. No.	Eigenvalues derived from linearized model	Eigenvalues derived from simulink model
1.	-8000	-8000
2.	$-3000 + 10^4$	$-3000 + 10^4$
3.	$-3000 - 10^4$	$-3000 - 10^4$
4.	-2200	-2200
5.	-2400	-2400
6.	$-1300 + 0.1*10^4$	$-1300 + 0.1*10^4$
7.	$-1300 - 0.1*10^4$	$-1300 - 0.1*10^4$
8.	$-1200 + 0.1*10^4$	$-1200 + 0.1*10^4$
9.	$-1300 - 0.1*10^4$	$-1300 - 0.1*10^4$
10.	$-300 + 0.5*10^4$	$-300 + 0.5*10^4$
11.	$-300 + 0.5*10^4$	$-300 + 0.5*10^4$
12.	-100	-100
13.	0	0
14.	100	100

3 Results and Discussion

The microgrid as shown in Figure 1 was simulated in MATLAB Simulink with model parameter reported in Table 1 and analysis was carried out to understand the challenges in microgrid system. System consist of 10 kW of solar PV module as source is connected at point of common coupling (PCC) with the grid of frequency 50 Hz and line to line voltage of 400 V and a 25 kVA of AC load. Under normal conditions microgrid works stable as shown in figures below. Figure 7 shows active and reactive power delivered from the source at normal operation of microgrid. It presents voltage at PCC in dq- frame and the corresponding currents in the same frame. It can be observed that reactive power supplied by sources is zero in steady state because controller has been designed such that V_q component is maintained at zero.

Grid voltage is crucial in grid connected microgrid system because DG controller is designed to track the grid voltage and to inject power into the network as required. In order to analyse the stability and dynamics of microgrid due to grid voltage disturbance, a 10% step change in grid voltage is introduced in the system at t = 1.5 secs. After applying the disturbance, it can be observed in Figure 8, that active power is stable in steady state while reactive power is zero as controller is maintaining I_q component of current at zero. A change of voltage (V_d) from 326 V to 359.18 V and of current (I_d) from 13.93 A to 12.66 A is reported at time t=1.5 sec as shown in figure below.
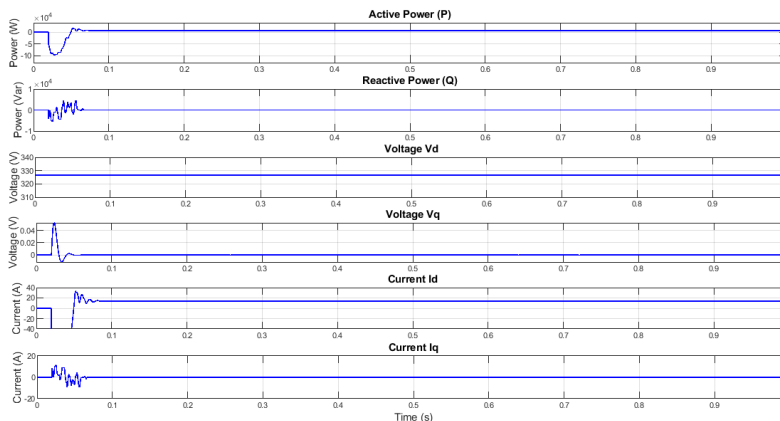
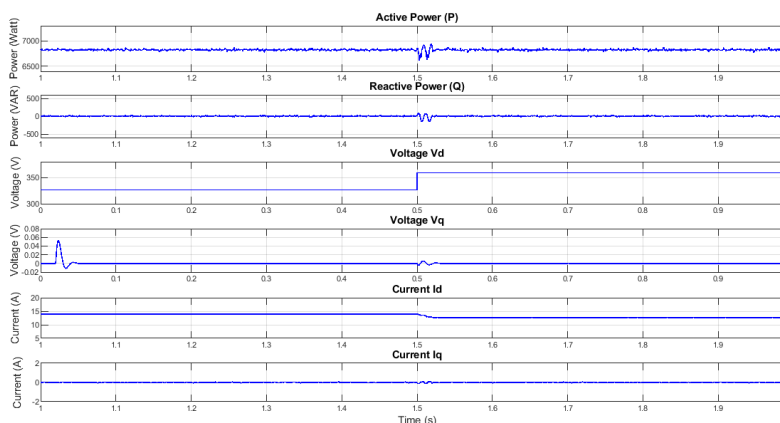**Fig 7. Power, Voltage and Current at PCC under normal conditions**

Fig 8. Power, Voltage and Current at PCC under Grid change

Load throw off phenomenon is a test to check dynamic stability of microgrid where a load is suddenly disconnected, it can cause instability in microgrid, affecting parameters like frequency and power quality. AC load of 25 kVA which is connected to microgrid has been removed at t = 1.5 sec. After removing the load, active and reactive power are stable and voltage disturbance at PCC in dq-frame are shown in Figure 9. After removing the load, network Active power (P) changed from -1369.25 W to 6936.08 W and Reactive power (Q) from -3162.31 Var to 1800.33 Var demonstrating transition of power from negative to positive took place which implies that source power is being injected to network.

The primary aim of this dynamic modelling was to ensure the transient voltage stability of the grid-connected microgrid under dynamic conditions through appropriate parameter design and control strategies. Unlike previous studies that primarily focused on steady-state analysis or neglected the dynamics of PLLs and LCL filters, this work comprehensively investigates the microgrid's stability during grid voltage fluctuations and load disturbances. During the simulation, a 10% grid voltage alteration was introduced, and the microgrid exhibited stable active and reactive power responses, with currents and voltages at the PCC stabilizing rapidly within 0.2 seconds, outperforming the limitations of previous works. Furthermore, a significant load disturbance was simulated by disconnecting a 25 kVA active load, a scenario that has been less explored in previous microgrid stability studies. The microgrid effectively managed the power transition within the network, as evidenced by the change from negative to positive power flow, indicating a shift in the direction of power flow from the solar source to the network. This seamless transition highlights the microgrid's ability to adapt to changes in load conditions while maintaining stable operation, a capability that has not been extensively demonstrated in previous research. The proposed control strategy, featuring a voltage controller to maintain the DC-link voltage at its desired reference value and a current controller operating in the d-q frame, played a crucial role in achieving robust transient voltage stability.
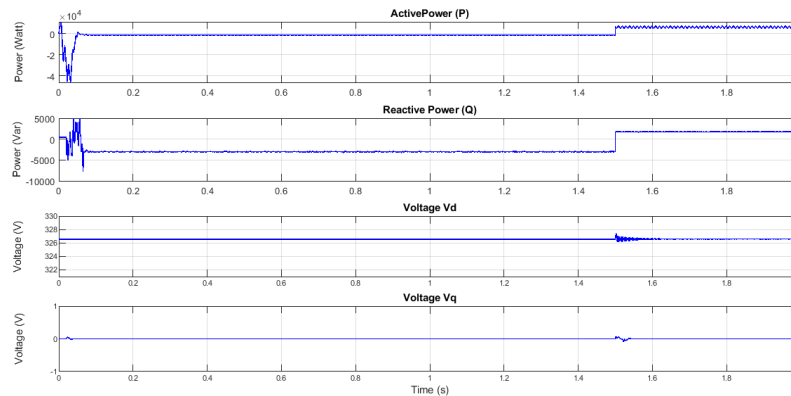
Fig 9. Power supplied by network and Voltage at PCC under load throw off

4 Conclusion

This study presents a comprehensive small-signal state-space model of a grid-connected inverter-based microgrid, addressing a critical research gap in the transient voltage stability analysis of microgrids under dynamic conditions. The novelty of this work lies in the development of a detailed model that incorporates the dynamics of inverters, phase-locked loops (PLLs), and LCL filters, elements that have been overlooked in previous studies. Furthermore, a robust control strategy featuring a voltage controller and a current controller operating in the d-q frame is proposed to enhance stable power conversion and maintain microgrid stability during transient events. The small-signal model was analysed through eigenvalue analysis, and the results were validated against MATLAB/Simulink simulations, ensuring the accuracy and reliability of the proposed approach. The current controller, a key component of the control strategy, simplifies AC current control by integrating active power management from the solar input, DC-link voltage stability, and reactive power control, outperforming the limitations of previous works. Through simulations, the microgrid's transient voltage stability was tested under severe dynamic conditions, including a 10% grid voltage fluctuation and the disconnection of a 25 kVA active load, scenarios that have received limited attention in previous microgrid stability studies. The obtained results demonstrate the microgrid's ability to maintain stable operation, with key parameters such as active and reactive power, currents, and voltages at the point of common coupling exhibiting rapid stabilization within 0.2 seconds during the grid voltage fluctuation. Furthermore, the microgrid effectively managed the power transition within the network during the load disturbance, seamlessly adapting to the change in load conditions while maintaining stable operation with minimal deviations in key parameters. The proposed control strategy, featuring the voltage and current controllers, played a crucial role in achieving these robust and quantifiable results, offering a novel approach to enhancing the resilience and reliability of grid-connected microgrids during transient events. The findings of this study pave the way for further advancements in microgrid control and stability analysis, contributing to the development of more resilient and reliable power systems capable of integrating renewable energy sources and distributed generation.

Acknowledgement

References

1) Saeed MH, Fangzong W, Kalwar BA, Iqbal S. A Review on Microgrids' Challenges & Perspectives. *IEEE Access*. 2021;9:166502–166517. Available from: https://dx.doi.org/10.1109/access.2021.3135083.
2) Jayaswal K, Palwalia DK, Sharma A. Renewable Energy in India and World for Sustainable Development. In: Bhaskar MS, Gupta N, Padmanaban S, Holm-Nielsen JB, Subramaniam U, editors. Power Electronics for Green Energy Conversion. Wiley. 2022;p. 67–89. Available from: https://doi.org/10.1002/9781119786511.ch3.
3) Ahmed K, Seyedmahmoudian M, Mekhilef S, Mubarak NM, Stojcevski A. A Review on Primary and Secondary Controls of Inverter-interfaced Microgrid. *Journal of Modern Power Systems and Clean Energy*. 2021;9(5):969–985. Available from: https://dx.doi.org/10.35833/mpce.2020.000068.
4) Jain D, Saxena D. Comprehensive review on control schemes and stability investigation of hybrid AC-DC microgrid. *Electric Power Systems Research*. 2023;218. Available from: https://dx.doi.org/10.1016/j.epsr.2023.109182.
5) Chaturvedi P, Palwalia DK. PMSG based Standalone Wind Energy Conversion System with Power Quality Enhancement. *International Journal of Renewable Energy Research*. 2023;13(2):911–919. Available from: https://doi.org/10.20508/ijrer.v13i2.13958.g8764.

6) Chartier SL, Venkiteswaran VK, Rangarajan SS, Collins ER, Senjyu T. Microgrid Emergence, Integration, and Influence on the Future Energy Generation Equilibrium—A Review. *Electronics*. 2022;11(5):1–21. Available from: https://dx.doi.org/10.3390/electronics11050791.

7) Mannini R, Eynard J, Grieu S. A Survey of Recent Advances in the Smart Management of Microgrids and Networked Microgrids. *Energies*. 2022;15(19):1–37. Available from: https://dx.doi.org/10.3390/en15197009.

8) Gonzales-Zurita Ó, Clairand JM, Peñalvo-López E, Escrivá-Escrivá G. Review on Multi-Objective Control Strategies for Distributed Generation on Inverter-Based Microgrids. *Energies*. 2020;13(13):1–29. Available from: https://dx.doi.org/10.3390/en13133483.

9) Rajamand S. Synchronous Generator Control Concept and Modified Droop for Frequency and Voltage Stability of Microgrid Including Inverter-Based DGs. *Journal of Electrical Engineering & Technology*. 2020;15(3):1035–1044. Available from: https://dx.doi.org/10.1007/s42835-020-00383-z.

10) Naraghipour K, Abdelsalam I, Ahmed KH, Booth CD. Modified Q–f Droop Curve Method for Islanding Detection With Zero Non-Detection Zone. *IEEE Access*. 2021;9:158027–158040. Available from: https://dx.doi.org/10.1109/access.2021.3130370.

11) AbdelAty AM, Al-Durra A, Zeineldin H, El-Saadany EF. Improving small-signal stability of inverter-based microgrids using fractional-order control. *International Journal of Electrical Power & Energy Systems*. 2024;156:1–15. Available from: https://dx.doi.org/10.1016/j.ijepes.2023.109746.

12) Mahdavian A, Ghadimi AA, Bayat M. Microgrid small-signal stability analysis considering dynamic load model. *IET Renewable Power Generation*. 2021;15(13):2799–2813. Available from: https://dx.doi.org/10.1049/rpg2.12203.

13) Maurya SS, Jain TC, Umarikar AC. Small-Signal Stability Analysis of Synchronverter-Based AC Microgrid in Islanded Mode. In: International Online Conference on Smart Grid Energy Systems and Control;vol. 1099 of Lecture Notes in Electrical Engineering. Singapore. Springer. 2024;p. 315–334. Available from: https://doi.org/10.1007/978-981-99-7630-0_24.

14) Alnuman H. Small Signal Stability Analysis of a Microgrid in Grid-Connected Mode. *Sustainability*. 2022;14(15):1–15. Available from: https://dx.doi.org/10.3390/su14159372.

15) Ahmadi H, Shafiee Q, Bevrani H. Dynamic modeling and transient stability analysis of distributed generators in a microgrid system. *International Journal of Electrical and Computer Engineering (IJECE)*. 2021;11(5):3692–3703. Available from: https://dx.doi.org/10.11591/ijece.v11i5.pp3692-3703.

16) Gali V, Jamwal PK, Gupta N. Stability enhancement of grid side converter in PV-wind-BESS based microgrid under weak grid conditions. *Electric Power Systems Research*. 2023;221. Available from: https://dx.doi.org/10.1016/j.epsr.2023.109481.

17) Wang X, Li J, Guo Q, Wang H, Ding Y. Parameter Design of Half-Bridge Converter Series Y-Connection Microgrid Grid-Connected Filter Based on Improved PSO-LSSVM. *International Transactions on Electrical Energy Systems*. 2023;2023:1–13. Available from: https://dx.doi.org/10.1155/2023/9534004.

18) Benlahbib B, Bouarroudj N, Mekhilef S, Abdeldjalil D, Abdelkrim T, Bouchafaa F, et al. Experimental investigation of power management and control of a PV/wind/fuel cell/battery hybrid energy system microgrid. *International Journal of Hydrogen Energy*. 2020;45(53):29110–29122. Available from: https://dx.doi.org/10.1016/j.ijhydene.2020.07.251.

19) Suyanto S, Mohammad L, Setiadi IC, Roekmono R. Analysis and Evaluation Performance of MPPT Algorithms: Perturb & Observe (P&O), Firefly, and Flower Pollination (FPA) in Smart Microgrid Solar Panel Systems. In: 2019 International Conference on Technologies and Policies in Electric Power & Energy. IEEE. 2020;p. 1–6. Available from: https://doi.org/10.1109/IEEECONF48524.2019.9102532.

20) Ahmad S, Mekhilef S, Mokhlis H. An improved power control strategy for grid-connected hybrid microgrid without park transformation and phase-locked loop system. *International Transactions on Electrical Energy Systems*. 2021;31(7). Available from: https://dx.doi.org/10.1002/2050-7038.12922.